1   Total Column Ozone Trends from the NASA Merged Ozone Time Series 1979 to 2021 Showing Latitude
2   Dependent Ozone Recovery Dates (1994 to 1998)

3   Jay Herman[1], Jerald Ziemke[2], and Richard McPeters[3]

[1]University of Maryland Baltimore County, Baltimore Maryland USA

[2]Morgan State University, Baltimore Maryland, USA

[3]NASA Goddard Space Flight Center, Greenbelt, Maryland, USA

Corresponding Author: Jay Herman   Herman@umbc.edu

17   **Abstract**

18   Monthly averaged total column ozone data $\Omega_{MOD}(t,\theta)$ from the NASA Merged Ozone Data set

19   (MOD) were examined to show that the latitude-dependent, θ, ozone depletion turnaround dates $T_A(\theta)$

20   range from 1994 to 1998. $T_A(\theta)$ is defined as the approximate date when the zonally average ozone

21   ceased decreasing. Ω_{MOD} data used in this study were created by combining data from Solar

22   Backscattered Ultraviolet instruments (SBUV/SBUV-2) and the Ozone Mapping and Profiler Suite (OMPS-

23   NP) from 1979 to 2021. The new calculated systematic latitude-dependent hemispherically asymmetric

24    $T_A(\theta)$ shape should appear in atmospheric models that combine the effects of photochemistry, volcanic

25   eruptions, and dynamics in their estimate of ozone recovery. Trends of zonally averaged total column

26   ozone in percent per decade were computed before and after $T_A(\theta)$ using two different trend estimate

27   methods that closely agree, Fourier Series Multivariate Linear Regression and linear regression on

28   annual averages. During the period 1979 to $T_A(\theta)$ the most dramatic rates of SH ozone loss were P_D = -

29   10.9 ± 3 % per decade at 77.5^{O}S and -8.5±0.9% per decade at 65°S, which is about double the NH rate of

30   loss of P_D = -5.6±4 %/decade at 77.5^{O}N and 4.4±1%/decade at 65°N for the period 1979 to $T_A(\theta)$. After

31    $T_A(\theta)$, there has been an increase at 65°S of P_D = 1.6±1.4% per decade with smaller increases from 55°S

32   to 25°S and a small decrease at 35°N of -0.4±0.3 %/decade. Except for the Antarctic region, there only

33   has been a small recovery in the Southern Hemisphere toward 1979 ozone values and almost none in

34   the Northern Hemisphere.

36

37

38   **1.0 Introduction**

39   Ozone is a photolytically produced, photochemically destroyed, and dynamically distributed
40   atmospheric gas that plays a crucial role in protecting the planet from harmful ultraviolet (UV) radiation
41   from the sun. The atmospheric presence of bromine and the release of chlorine from the UV
42   dissociation of man-made chemicals, such as chlorofluorocarbons (CFCs), can break down the ozone
43   layer at all latitudes. This is especially the case in the Antarctic region where heterogeneous chemistry
44   on and within ice crystals and liquid droplets (Tritscher, et al., 2021) in polar stratospheric clouds PSCs
45   have a strong effect on the destruction of ozone during September and October (WMO, 2022; Tritscher,
46   et al., 2021; Solomon et al., 1986; 1999; 2016; Crutzen and Arnold, 1986; Khosrawi et al., 2011). As the
47   sun rises in Spring, chemically active nitrogen oxides, chlorine and bromine are released causing the
48   ozone hole to develop within the region enclosed by the polar vortex winds. The weak levels of sunlight
49   are sufficient to initiate and maintain the catalytic ozone loss photochemistry. In November and
50   December, the isolating polar vortex winds break down and the Antarctic ozone hole region back fills by
51   air exchange from southern mid-latitudes causing $T_A(35^OS – 65^OS)$ to be delayed compared to the
52   Northern Hemisphere NH mid-latitudes. The recurring annual ozone hole event triggered international
53   action to limit the production and use of ozone-depleting substances (ODS) under the Montreal
54   Protocol, which has been successful in reducing the emission of these substances, slowing down the
55   depletion of the ozone layer globally, leading to a partial recovery in the Antarctic ozone hole region
56   (Solomon et al., 2016; Strahan and Douglass 2018). After the mid-1990s, several studies have reported
57   an increase in total column ozone (TCO), particularly in the mid to high latitudes of the Southern
58   Hemisphere, as well as a reduction in the size and depth of the Antarctic ozone hole starting in the late
59   1990s (Solomon et al., 2016; Stone et al., 2018; 2021, Weber et al., 2022).

60   The cessation of ozone decrease was first observed in the mid-1990s when satellite data showed a
61   stabilization and slight increase in ozone concentrations in the Antarctic ozone hole region. However,
62   the recovery was not significant enough to be considered a trend at that time (Strahan and Douglass
63   2018). In the early 2000s, further analysis of satellite and ground-based data showed that the rate of
64   ozone depletion had slowed down. After the mid-1990's, the cessation of ozone depletion has been
65   most evident in the Southern Hemisphere SH polar region, where ozone depletion had been most
66   severe. Ozone recovery has been slow or non-existent at other latitudes. Recently, Weber et al. (2022)
67   showed reduction in ozone at all latitudes prior to 1995 and reported positive statistically significant
68   TCO trends from 1996-2020 at southern middle and high latitudes, and over the SH polar cap in
69   September. When dynamical terms were included in the regression, small positive trends were near the
70   2-standard deviation 2σ threshold at northern mid- and high-latitudes, with no trend detected in the
71   tropics or over the NH polar cap.

72   Despite the success of the Montreal Protocol (Velders and Andersen, 2018), ozone concentrations
73   continue to fluctuate, driven by natural and anthropogenic factors, such as, changes in solar radiation,
74   stratospheric circulation, global warming, volcanic activity, and changing emissions of ozone precursors
75   (Dameris and Baldwin, 2012; Weber et al., 2022). The discussion by Dameris and Baldwin (2012)
76   explored possible effects of climate change on the dynamics of the atmosphere affecting ozone as ODSs
77   change, and particularly the change in the Brewer-Dobson circulation (Brewer, 1949; Dobson et al.,

78 1926) that transports ozone from an upwelling in the equatorial region into the stratosphere and to
79 downwelling into mid- and high-latitudes.

80 This study will estimate new latitude dependent ozone recovery dates, or more accurately the dates of
81 cessation of ozone decrease, $T_A(\theta)$ ranging from 1994 (equatorial region and 60^ON to 70^ON) to 1998
82 (60^OS – 80^OS). The calculated $T_A(\theta)$ and ozone trends (%/decade) include the effects of volcanic
83 eruptions such as Mt. Pinatubo in 1991, dynamics, and atmospheric temperature changes. Ozone data
84 used in this study are a subset of the Merged Ozone Data MOD set $\Omega_{MOD}(t)$ (1970 – 2021) starting in
85 1979 with the Nimbus-7 SBUV (Solar Backscattered Ultraviolet) satellite instrument. From 1979 to 2021,
86 the MOD data set was created by combining data from Solar Backscattered Ultraviolet instruments
87 (SBUV/SBUV-2) and the Ozone Mapping and Profiler Suite (OMPS-NP). Methods of calculating trends
88 from time series data are essential in the analysis of environmental and climate-related data. Here, we
89 discuss two independent methods to estimate linear trends: 1) linear regression of annual averaged
90 data and 2) Fourier time series decomposition or multivariate linear regression MLR (Ziemke et al.,
91 2019) are discussed below. The two methods are compared and shown to give nearly identical results
92 over their mutual latitude range of validity, 65^OS to 65^ON. The MLR method is not used in the regions
93 poleward of the Arctic and Antarctic circles that have latitude dependent extended winter polar night.
94 The advantage of the MLR method (Eq. 1), or that in Weber et al, 2002, is that it can be used to estimate
95 the effects of its individual components, while the annual average method can be used in the polar
96 regions where there is latitude dependent extended winter night.

97 **1.1 The Merged Ozone Data Set MOD**

98 Figure 1 (left panel) shows the MOD zonally averaged Ω_{MOD} TCO data (Frith et al., 2014; 2020) set as a
99 function of latitude (5° latitude bands from 77.5^OS to 77.5^ON) and time (January 1979 to December
100 2021). Part of the Antarctic ozone hole (75^OS to 80^OS) is shown (blue color), and the high latitude
101 maxima, North and South, (red color), with low values in the equatorial region. Figure 1 (right panel)
102 shows the 42-year zonal and time averaged ozone amounts and the maxima and minima annual
103 envelopes as a function of latitude. Figure 1 shows the asymmetry in the monthly and zonally averaged
104 ozone data between the hemispheres, with the Northern Hemisphere NH having more ozone than the
105 Southern Hemisphere SH at corresponding latitudes. Part of the asymmetry is driven by the Spring
106 Antarctic ozone hole backfilling in the SH summer.
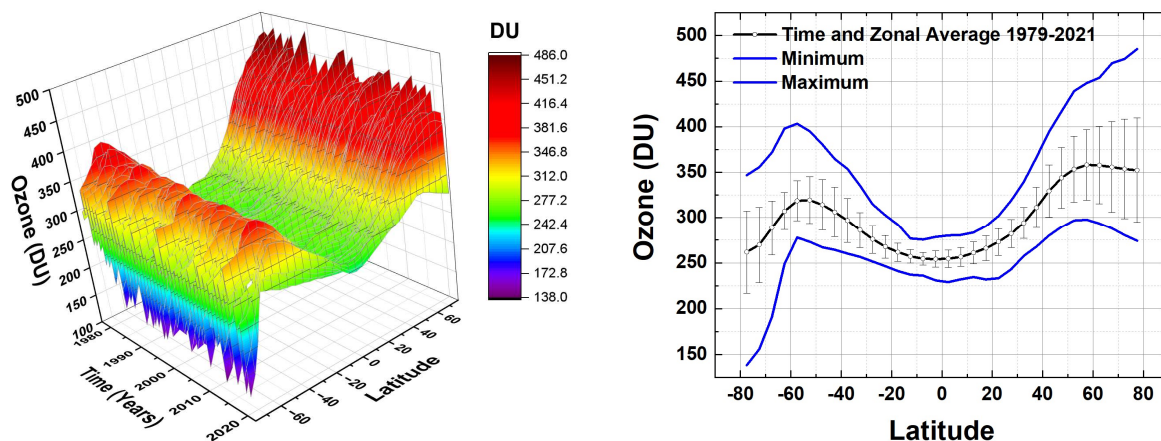
Fig. 1 Left: The zonally and monthly averaged Ω_{MOD} data set 1979 – 2021 and -77.5^O to 77.5^O. Right: Time and zonal averaged ozone and its maxima and minima 1979 – 2021. Error bars are 1 standard deviation ±1σ.

107 $\Omega_{MOD}(t,\theta)$ provides a global view of ozone levels needed to track changes in ozone concentrations over
108 time t for each latitude band θ. The SBUV and OMPS-NP series of satellite instruments form the longest
109 (1979 to 2022) continuous global ozone $\Omega_{MOD}(t,\theta)$ data record from a single instrument type. Merged
110 ozone retrievals from the individual instruments use the version 8.7 retrieval algorithm (described by
111 Weber et al., 2022) as an extension of the version 8.6 algorithm (Bhartia et al., 2013; McPeters et al.,
112 2013; DeLand et al., 2012; Frith et al., 2017) specifically designed to improve cross calibrations between
113 the later SBUV-type instruments in MOD starting from NOAA-16 in 2000. There were no external
114 adjustments made to the ozone retrieval except for small high-altitude (> 35 km) diurnal corrections to
115 account for different measurement times between satellites and varying measurement time of day as
116 individual satellite orbits slowly drift in equator crossing time. These adjustments are very minor in TCO
117 (Frith, personal communication). Data from each instrument are selected based on quality criteria
118 outlined in Frith et al. (2014; 2020) and the data are averaged during periods when more than one
119 instrument was operational. The $\Omega_{MOD}(t,\theta)$ are available as a function of latitude and month,
120 https://acd-ext.gsfc.nasa.gov/Data_services/merged/.
121
122 Analysis of the long-term ozone time series has been looked at extensively with references given in
123 Weber et al., 2022. Methods for estimating trends from an oscillating time series with several distinct
124 periodicities are well known (Ziemke et al., 2019; Stolarski et al. 1991;1992, Herman et al., 1993). For
125 ozone, one of the difficulties in trend estimation is that the early part of the time series shows a strong
126 ozone decrease at all latitudes that continued until the mid-1990s and then flattens out and shows
127 almost no recovery thereafter toward 1979 values. The Ω_{MOD} time series has been used extensively in
128 ozone assessments and State of the Climate reports (e.g., WMO, 2022) and was recently compared to
129 several other merged total ozone records in Weber et al. (2022). The validity of the Ω_{MOD} time series for
130 estimating ozone trends was further checked (See Appendix Figs. A1 to A3) in this study by showing
131 detailed comparisons between the deseasonalized Ω_{MOD} time series with the deseasonalized MLS
132 (Microwave Limb Sounder) overlapping stratospheric ozone time series (2005 to 2023).

133 **2.0 Trend Estimates from the MOD Ozone Data**

134 Multivariate Linear Regression MLR is a Fourier based method for analyzing atmospheric time series
135 data that decomposes the time series into its component parts, including trend, quasi-biennial
136 oscillation QBO, solar cycle, ENSO (El Nino Southern Oscillation), seasonality, and noise resulting in a
137 trend estimate and 2-standard deviation 2σ uncertainty estimates (Ziemke et al., 2019). Calculated 2σ
138 uncertainties for the MLR trends include a first order autoregressive adjustment applied to the derived
139 residuals (Weatherhead et al., 1998).

140 Linear trend estimates for the long-term changes in $\Omega_{MOD}(t, \theta_i)$ globally and as a function of latitude θ_i
141 have been obtained using the multivariate linear regression (MLR) model (e.g., Randel and Cobb, 1994,
142 and references therein). Trends $B(\theta_i)$ were determined for $\Omega_{MOD}(t, \theta_i)$ using Eqns. 1 and 2.
143

$$\Omega_{MOD}(t, \theta_i) = A(\theta_i\ t) + B(\theta_i,t)\cdot t + C(\theta_i,t)\cdot QBO_1(t) + D(\theta_i,t)\cdot QBO_2(t) + \qquad (1)$$
$$E(\theta_i,t)\cdot ENSO(t) + F(\theta_i,t)\cdot Solar(t) + R(t, \theta_i)$$

144
145 where t is the month index (t=1 to 516 months with data for 1979–2021), $A(\theta_i\ t)$ is the seasonal cycle
146 coefficient, $B(\theta_i,t)$ is the trend coefficient, $C(\theta_i,t)$ is the first empirical orthogonal function (EOF) QBO
147 coefficient, $D(\theta_i,t)$ is the second EOF QBO coefficient, both representing the major components of
148 the QBO variability, $E(\theta_i,t)$ is the ENSO coefficient, $F(\theta_i,t)$ is the solar cycle coefficient, and R(t) is the
149 residual error time series. The F10.7 cm solar flux monthly time series is used for the Solar(t) proxy, first
150 and second leading EOF QBO monthly time series proxies $QBO_1(t)$ and $QBO_2(t)$ are used for the QBO
151 component (Wallace et al., 1993), and Nino 3.4 (Oldenborgh *et al* 2021) is used for ENSO(t) (Nino 3.4:
152 https://www.ncei.noaa.gov/access/monitoring/enso/sst). $QBO_1(t)$ and $QBO_2(t)$ are nearly orthogonal
153 (correlation coefficient approximately zero) oscillating time series based on data with approximately a
154 2.3-year periodicity. $A(\theta_i,t)$ involves 7 fixed constants while $B(\theta_i,t)$ (and all other remaining coefficients)
155 involves 5 fixed constants for each θ_i. The harmonic expansion for A(t) (similar for the other
156 coefficients) is (Eqn. 2).
157

$$A(t) = a(0) + \sum_{p=1}^{3}\left[a(p)\cos(2\pi p t / 365) + b(p)\sin(2\pi p t / 365)\right] \qquad (2)$$

158
159 where a(p) and b(p) are constants. Statistical uncertainties for A(t) and $B(\theta_i)$ were derived from the
160 calculated statistical covariance matrix involving the variances and cross-covariances of the constants
161 (e.g., Guttman et al., 1982; Randel and Cobb, 1994).
162
163 In this study the Locally Weighted Scatterplot Smoothing Lowess(f) least-squares technique is used to
164 reduce oscillations in the time series data and to estimate $T_A(\theta)$where f = the fraction of data averaged
165 together (Cleveland, 1979 and Cleveland and Devlin, 1988).

166
167
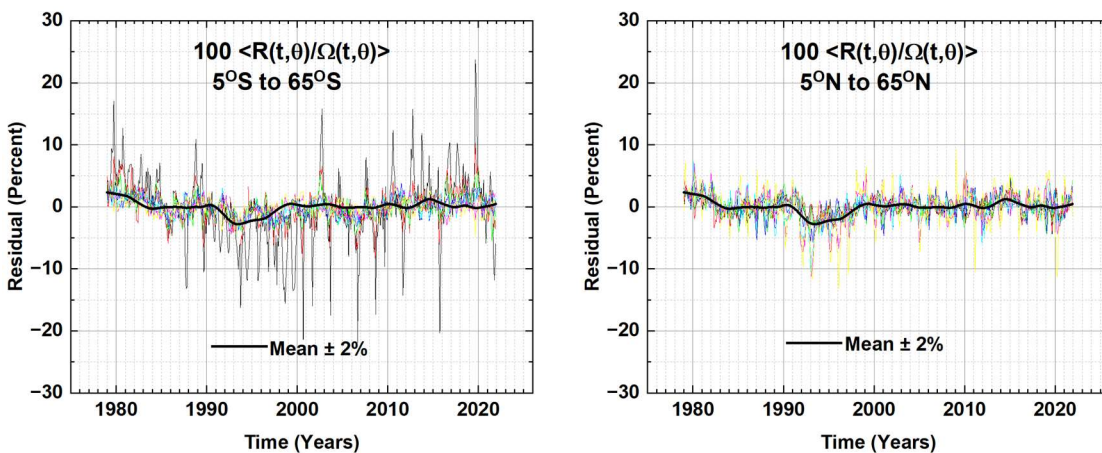
Fig. 2 The latitude average residual term from Eq. 1 in percent 100 <R(t,q$_i$)/W$_{MOD}$(t,q$_i$)> The black line
is the Lowess(0.1) fit (Cleveland, 1979) to the R(t,q) with an average error estimate of ±2%. The light-
colored lines are each latitude's R(t,q) in a hemisphere 0° < θ < 65°.

168

169 The latitude average residual R(t) in percent of the MOD ozone amount (100 <R(t,θ$_i$)/ Ω$_{MOD}$(t,θ$_i$)>) is shown

170 in Fig. 2 for the SH and NH as an indication of how well Eq 1 is able to fit the Ω$_{MOD}$(t,θ$_i$) time series.

171

172 The SH R(t,θ) is more variable than the NH with the largest variations arising in the 55°S and 65°S latitude

173 bands. On average Eq. 1 fits the original data Ω$_{MOD}$(t,θ$_i$) to within ±2%.

174

175 The linear deseasonalized trend results B(θ$_i$) are obtained for 14 latitude bands θ$_i$ (centered on 65°S to

176 65°N). The latitudinal trends P$_D$(θ$_i$) are expressed in %/Decade given by Eq. 3, where the denominator D

177 is either the time average <Ω> of the area weighted global ozone average (Fig 1) or the time average D(θ$_i$)

178 = < Ω$_{MOD}$(t, θ$_i$)> for each latitude band over the considered period. The whole year period considered is

179 1979 – 2021.

180

$$P_D(θ_i) = 1000 \, B(θ_i) \, /D(θ_i) \quad (\% \, / \, \text{Decade}) \qquad (3)$$

181

182 In the second method, the trend is estimated using annual integrals (annual averages) that remove the

183 seasonality and other short-term oscillations but ignore longer term oscillations such as the 28-to-29-

184 month QBO cycle and the average 11.3-year solar cycle. A comparison of the two trend estimating

185 methods is shown in Fig. 3 for the entire 1979 to 2021 period showing that they agree quite closely, but

186 that the annual average method has slightly larger two standard deviations 2σ than the MLR method.

187

188 The MLR method (Eqns. 1 and 2) are not applied poleward of the Arctic and Antarctic circles where

189 latitude dependent extended winter night periods occur. Additional latitude dependent terms of varying

190 periods would be needed for latitudes greater than 70°. The annual average method does not have

191 these complications.

192
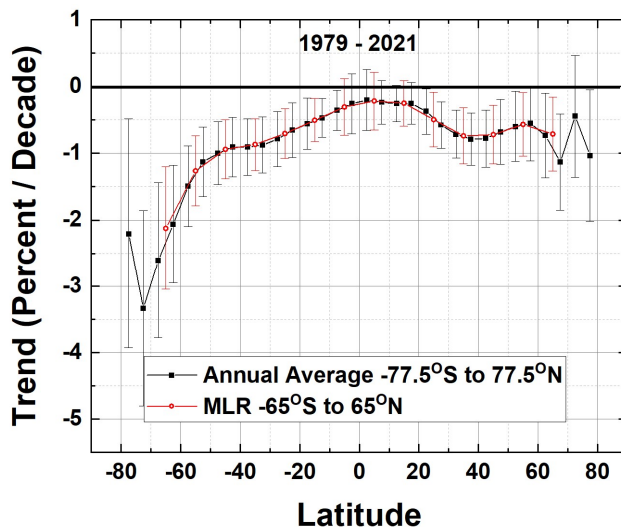
Fig. 3 The ozone trend $P_D(\theta)$ for the entire period 1979 – 2021 for two methods, MLR and Annual Average. The latitude grids for the two methods are offset to show the agreement in the trends and 2σ error bars.

193

194   The Fig. 3 estimation of linear long-term trends since 1979 is misleading, since ozone showed significant
195   annual declines until the mid-1990s and then increased slightly thereafter, meaning the average long-
196   term time series is non-linear. The usual procedure is to determine linear trends separately before and
197   after the turnaround dates T_A (Weber et al., 2022). However, as is shown later, there is no single
198   turnaround date applicable to all the latitudes between 80°S and 80°N. Instead, there is a range
199   spanning 1994 to 1998.
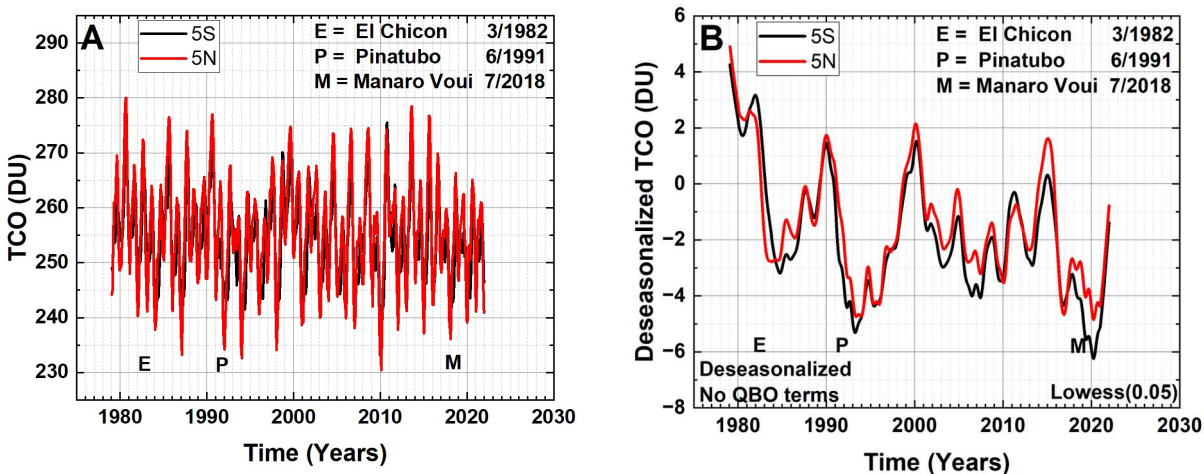
Fig. 4. A. Ω_{MOD} time series for $\theta = 5°N$ and $5°S$. B. The deseasonalized TCO time series for $\theta = 5°N$ and $5°S$ without removing QBO effects (Eq. 1). The approximate dates are shown of volcanic eruptions that injected large amounts of SO_2 into the stratosphere leading to minima approximately 1 year later.

200

201   Figure 4A shows the Ω_{MOD} time series for 5°S and 5°N, and Fig. 4B the deseasonalized and smoothed
202   (Lowess(0.05)) Ω_{MOD} time series. After deseasonalizing, but not removing QBO effects (Eq. 1), both the
203   2.3-year QBO oscillation and the reduced ozone effects from volcanic eruptions, are shown in Fig. 4B.
204   Some volcanos (e.g., from El Chicon March 1982, Mt. Pinatubo June 1991, and Manaro Voui July 2018)
205   inject significant amounts of SO$_2$ into the lower stratosphere leading to the formation of aerosols that
206   reduce UV light and the production of ozone, especially in the equatorial region.

207   Figure 5 shows the Lowess(0.3) fits (black curves) to the Ω_{MOD} data for four sample latitude bands 55°S,
208   45°S, 55°N, and 45°N that tracks the longer-term changes in the Ω_{MOD} time series. Also shown are
209   examples of f = 0.1 (red) and f = 0.05 (blue dots). The Lowess(0.05) fit (blue dots) shows considerable
210   structure with a minimum in 1993 that is likely related to the Mt. Pinatubo eruption and a modest El
211   Nino effect in 1991-1992.The estimated values of T$_A$ for f = 0.1 and 0.05 can differ by 6 months from that
212   determined when f=0.3 because of short term oscillations. The Lowess(0.3) degree of smoothing
213   removes most of the short-term effects on ozone such as QBO and those from volcanic eruptions from
214   El Chichon (1982) and Mt. Pinatubo (1991), both well before the earliest estimated T$_A$ in 1994.
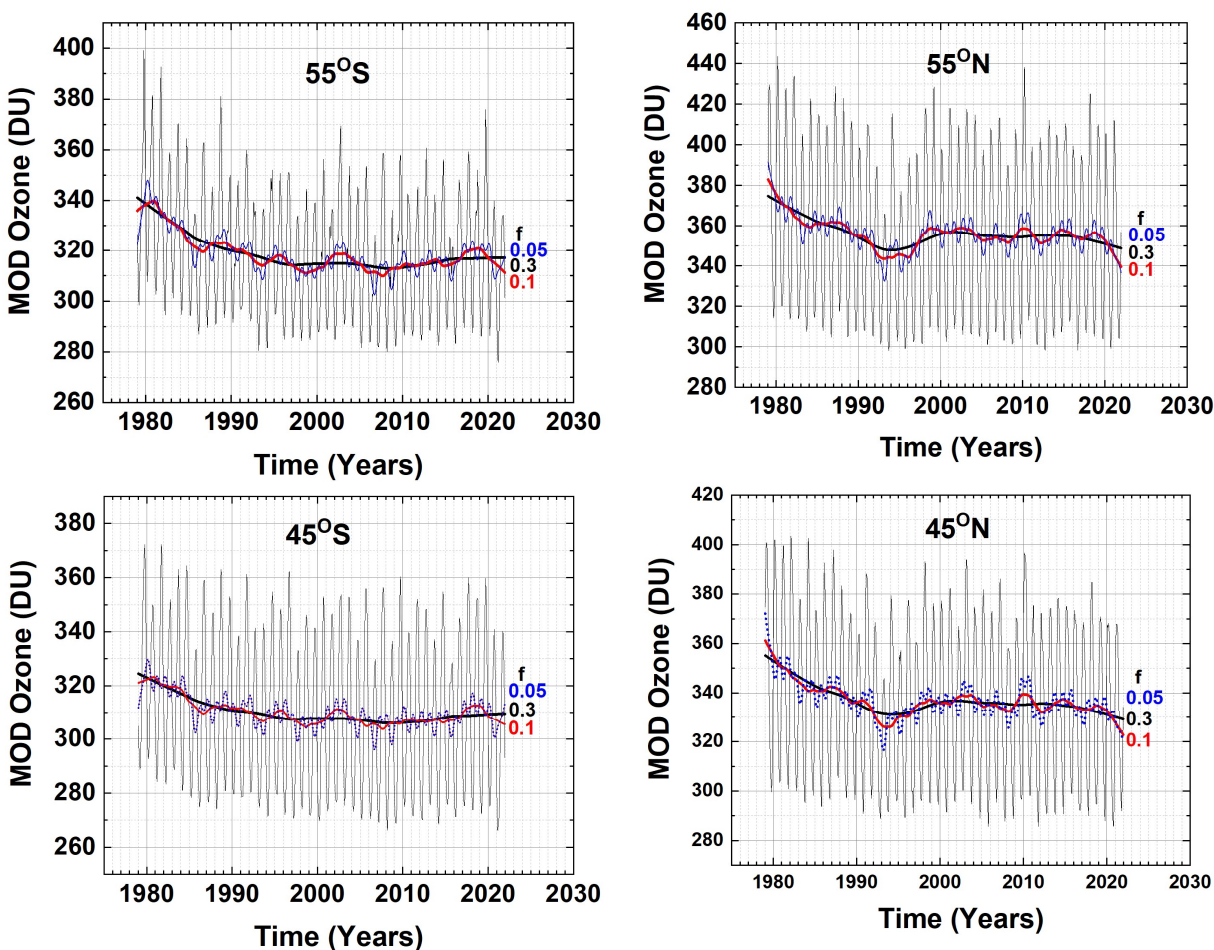
Fig. 5 Ω_{MOD} in four latitude bands and Lowess(0.3) fitting functions (f = 0.3, black lines). Examples of
different f = 0.1 (Red) and 0.05 (blue dots) are shown at 45°S and 45°N. Note the slight downturn
since 2010 in the Lowess(0.3) at 45°N and 55°N.

215   Figure 6 shows the Lowess(0.3) fits to the Ω_{MOD} data (1979 to 2021) for 16 latitude bands, $-75^O < \theta < 75^O$

216   on an expanded ozone scale. Each of the Lowess(0.3) plots for the various latitudes shows different

217   periods of ozone decrease and subsequent turnaround $T_A(\theta)$ after the mid-1990's. Use of expanded

218   ozone scales appears to show a sharp downturn after 2010 at some latitudes (25^ON to 75^ON). As shown

219   later, the apparent downturns in the Lowess(0.3) fit to Ω_{MOD} after 2010 are not yet statistically

220   significant in trend estimates from Ω_{MOD} as an indicator of long-term ozone decrease.
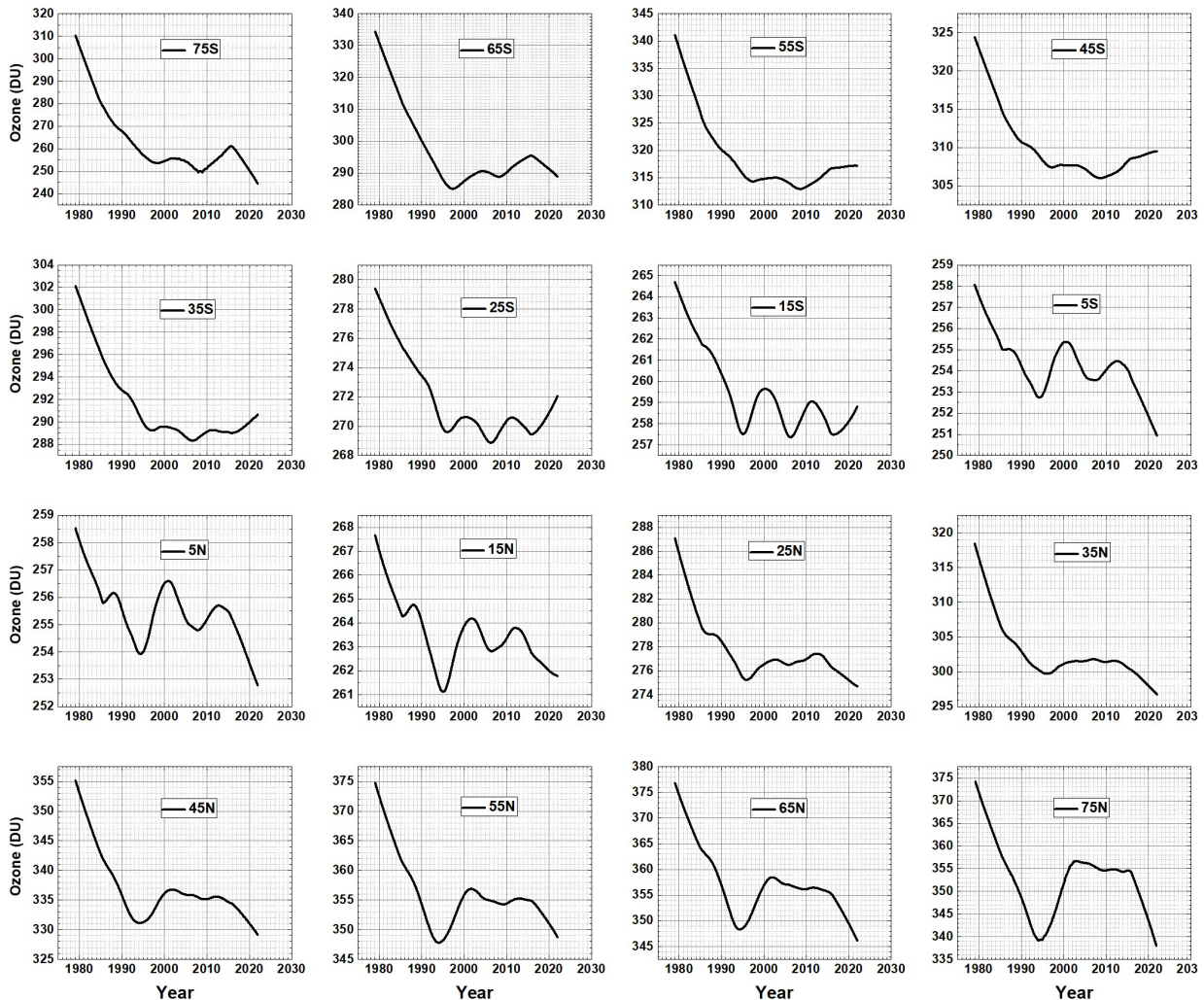
Fig. 6 Lowess(0.3) fits to the Ω_{MOD} data for 16 latitude bands used to determine $T_A(\theta)$. Note that the ozone scale varies for each latitude.

221   Figure 7 shows the turnaround dates $T_A(\theta)$ that are obtained by taking the 1st derivatives of Fig. 6 data

222   and finding the zero-crossing time corresponding to the appropriate minimum value in Fig. 6. The exact

223   turnaround dates determined have a precision of ± 0.1 years and an accuracy of ± 0.5 years. The ± 0.5

224   uncertainty does not affect the calculation of trends before and after the estimated $T_A(\theta)$. What is

225   interesting is that some of the turnaround dates in Fig. 7 are separated by over 4 years and are strongly

226   asymmetric between the hemispheres. Figure 7 shows a near symmetry for early turnaround dates

227   1994-1996 for low latitudes between ±25° that corresponds to the Brewer-Dobson ozone upwelling

228   region (Brewer et al., 1926; Dobson, 1949; Butchart, 2014) where most of the ozone is created by

229   sunlight and then transported poleward. At poleward latitudes, the turnaround dates are quite

230   different, with a delayed date, 1997, at high SH latitudes (35°S – 65°S), 1998 at 75°S compared to 1994

231   at high NH latitudes (45°N to 75°N).

232   The T_A delay to 1997 for latitudes 35°S – 65°S follows the delayed recovery of ozone depletion within

233   the Spring Antarctic Ozone Hole (Solomon, 1990; Stone et al., 2021, their Fig. 3; Bodeker and Kremser,

234   2021, their Figs. 6 and 9) and backfilling (air exchange with lower latitude ozone-rich air) during the

235   summer months after the polar vortex winds break down in October – November.

236
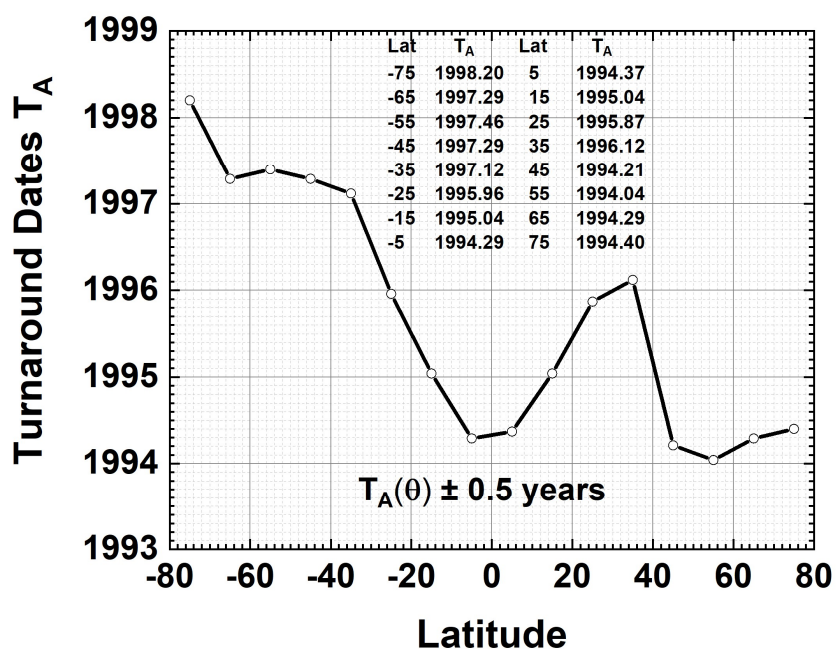
Lat	T_A	Lat	T_A
-75	1998.20	5	1994.37
-65	1997.29	15	1995.04
-55	1997.46	25	1995.87
-45	1997.29	35	1996.12
-35	1997.12	45	1994.21
-25	1995.96	55	1994.04
-15	1995.04	65	1994.29
-5	1994.29	75	1994.40

Fig 7 Turnaround dates $T_A(\theta)$ as a function of latitude from Fig.6 with an estimated accuracy of ±0.5
years based on the analysis in Fig. 5.

237

238   The general $T_A(\theta)$ pattern shown in Fig. 7 should appear in model calculations as a signature of the

239   combined effects of photochemistry, dynamics, and volcanic eruptions on the cessation of decreasing

240   ozone in the mid-1990s.
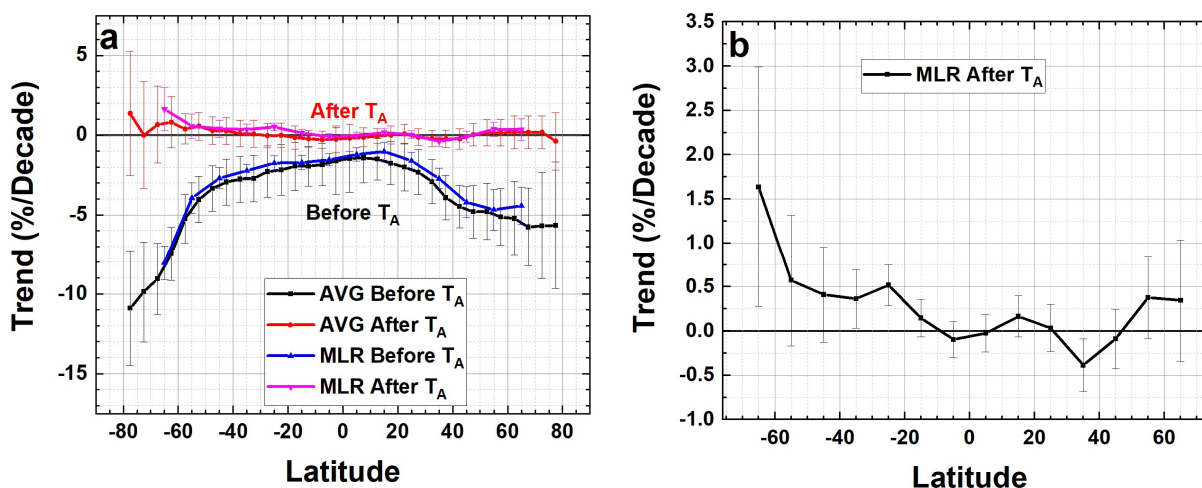
Fig. 8a Ozone trends $P_D(\theta)$ (percent per decade) using the MLR and Annual Average methods before and after $T_A(\theta)$. 6b A magnified version of the MLR estimated trends after T_A with 2σ uncertainties.

241

242   Trends (linear slopes) $P_D(\theta)$ in percent per decade are estimated (Eqn. 3) for the separate periods before

243   and after $T_A(\theta)$ in each latitude band (Fig. 8) and for the entire period (Fig. 3). The linear slopes obtained

244   by the two methods, MLR and annual average closely agree (Figs. 3 and 8) with the annual average

245   method extended to polar latitudes (Fig. 8a). Table 1 contains the data from Figs. 8a and 8b.

Table 1 MLR Trends (%/decade) ± 2σ

Latitude	P_D Before T_A	P_D After T_A
-65	-8.04±1.1	1.64±1.4
-55	-3.93±1.0	0.57±0.7
-45	-2.69±0.7	0.41±0.5
-35	-2.22±0.4	0.36±0.3
-25	-1.75±0.5	0.52±0.2
-15	-1.71±0.4	0.15±0.2
-5	-1.54±0.4	-0.10±0.2
5	-1.21±0.4	-0.03±0.2
15	-1.01±0.6	0.16±0.2
25	-1.61±0.5	0.03±0.3
35	-2.71±0.6	-0.39±0.3
45	-4.20±1.0	-0.09±0.3
55	-4.67±1.3	0.38±0.5
65	-4.43±1.2	0.35±0.7

246

247   The latitude dependent trends derived by Weber et al. (2022) using 1996.5 as the approximate T_A (their

248   Fig. 3) agree within error bars with the trends shown in Fig. 8 for all latitudes but they suggest T_A = 2000

249   for the polar regions. The trends also agree within error bars with those in WMO (2022). As mentioned

250   earlier, the trend estimates are not very sensitive to the exact T_A, but the shape of $T_A(\theta)$ should be a
251   model validation marker contained in model calculations for all effects, not just ODSs.

252   The delayed (1997) Southern Hemisphere mid and high latitude values of T_A are caused by coupling to
253   the increasing Antarctic spring ozone loss after 1979 until a recovery starting in about 1998-2000
254   (Solomon et al., 2016). The mid and high latitude, from 35°S to 65°S, delay is caused by the summer
255   mixing of ozone poor air from the Antarctic region with SH midlatitude ozone-rich air once the polar
256   vortex winds break down in November-December.

258   The asymmetry between the Arctic and Antarctic is caused by the lower winter Antarctic temperatures
259   (-80°C) leading to the formation of low altitude clouds containing ice crystals along with the isolating
260   Antarctic polar vortex winds (Solomon et al., 2007; 2016). In the spring sunlight the ice and water
261   droplets (Tritscher, et al., 2021) release ODS and depletes ozone to a monthly average of about 155 DU.
262   During the summer, air exchange with ozone rich air from lower latitudes comes into the polar latitudes and fill
263   in the ozone layer above Antarctica (monthly average about 300 DU. Smaller but significant ozone losses
264   occurred in the Artic region caused by occasional low temperatures and ODSs. The Arctic does not
265   routinely have the low temperatures needed for winter ice clouds nor does it have the persistent
266   isolating polar vortex winds because of wave action forced by the land topography The latitude band at
267   75°N (Fig.1) has the highest amount of monthly average winter ozone 450±25 DU that decreases to
268   290±20 DU monthly average during the summer that are comparable to mid-latitude values. The result
269   is earlier values of T_A in the NH compared to the SH. The NH T_A is earlier than the 1997 minimum in
270   stratospheric halogens (Weber et al., 2022; Newman et al., 2007). Note that T_A is not the time of the
271   start of recovery, but rather the time for the end of rapid ozone decrease.

273   Before the SH T_A, total column ozone decreased at a rate of P_D= -10.9±3.6% at 77.5^{O}S and -8.0±1.1% per
274   decade at 65°S, during the period from 1979 to 1997 with smaller decreases from 55°S to 25°S (Fig. 8a).
275   After the turnaround period T_A, ozone at 65°S increased at P_D = 1.6±1.4%/decade based on the MLR
276   method. After T_A, most other latitudes (Fig. 8b) show stationary ozone amounts within 2σ. In the NH the
277   decreases were smaller than in the SH before T_A because of the absence of an Arctic ozone hole region.
278   At 77.5^{O}N was P_D = -5.6±4%/decade and at 65°N P_D = -4.4±0.35 %/decade.

279   An analysis of ozone trends prior to the start of reliable satellite data in late 1978 showed that the
280   annual rate of ozone loss (%/Year) increased after 1978 (Staehelin et al., 2001). Based on the first
281   derivatives of the data in Fig. 6, the maximum annual rate of ozone reduction occurred in 1979 and 1980
282   in the NH and SH (Fig. 9) except for 65°N in 1992 where the rate of loss is -8.75%/Year. The loss rates
283   range from -20.6 %/Year at 75°S to 2.39 %/Year at 5°N. A smaller loss rate occurred for 35°N to 75°N
284   where the loss rate is almost constant between 8%/Year and 10%/Year compared to the larger SH loss
285   rates caused by the presence of the springtime Antarctic ozone hole.
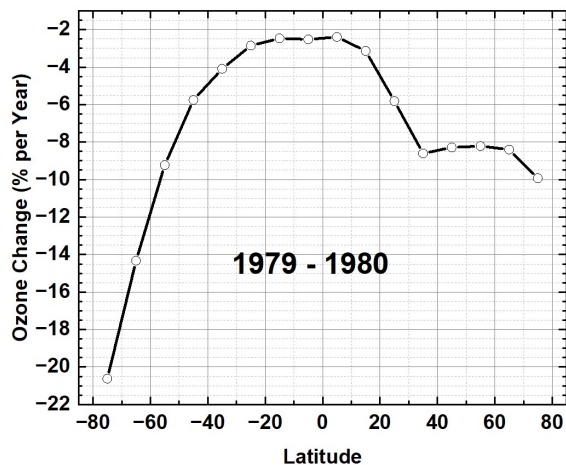
Fig. 9 The percent change in ozone per year in 1979 or 1980

286

287 The Lowess(0.3) plots in Fig. 6 suggest that Ω_{MOD} has been declining since approximately 2010 from 5^OS

288 to 65^ON but still increasing from 45^OS to 65^OS (Fig. 6). However, computing the trends (Fig. 10) from

289 $\Omega_{MOD}(t,\theta)$ using either the MLR (Eq. 1) or annual average methods suggest that the declines in ozone

290 from 25^OS to 65^ON are not yet significant at the 2σ level over the period 2010 – 2021.

291
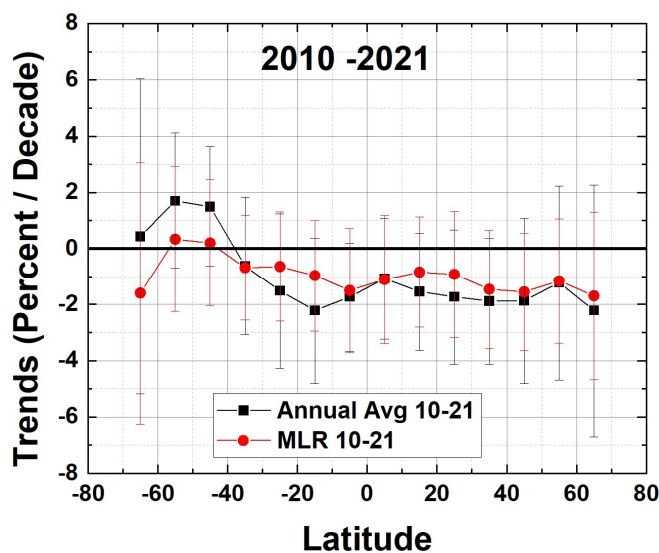
Fig. 10 Ozone trends $P_D(\theta)$ (Percent per Decade) for the period 2010 – 2021 for the Annual Average and MLR methods applied to $\Omega_{MOD}(t,\theta)$.

292 Comparing deseasonalized $\Omega_{MOD}(t,\theta)$ with deseasonalized Microwave Limb Sounder MLS (see Appendix

293 Figs. A1, A2, and A3) Stratospheric Ozone from 2005 to 2021 shows small average (Lowess(0.3))

294 differences that are within ±1DU except for 2021 when the differences at both 65^OS and 65^ON are about

295 -2.5DU. This suggests that the calibrations of the later SBUV-2 and OMPS-NP instruments are stable. For

296 2016 to 2018, Ω_{MOD} is obtained from NOAA-19 SBUV plus OMPS-NP and from just OMPS-NP since 2018.
297 Figure A3 suggests that there was a decrease in tropospheric ozone in 2020 that may correspond to
298 reduced economic activity during the COVID-19 pandemic.

299 Age of air AoA is a measure of how long a parcel of air resides in the stratosphere after it leaves the
300 troposphere (Linz et al., 2016; Ploeger et al, 2021). A comparison of T_A with AoA estimates from the
301 relatively inert tracer gas CO_2 (Fig. 11) for the altitude range near the ozone maximum (approximately
302 20 km) vs latitude (based on Waugh and Hall, 2002, their Fig. 6a and Ploeger et al, 2021 their Fig. 10a)
303 shows near symmetry between the hemispheres with the shortest AoA in the equatorial region. The
304 turnaround dates T_A in Fig. 6 are also symmetric in the equatorial zone corresponding the upwelling
305 Brewer Dobson circulation and the smaller AoA. This suggests that the combined effects of chemistry
306 and dynamics on ozone amounts are similar between ±25°. The precursors to ODS are also lifted into
307 the equatorial stratosphere and transported towards the polar regions (Newman et al., 2004; 2007)
308 where they can be photo-dissociated into ODS. Ozone at higher latitudes, NH and SH, with longer AoA,
309 will be dependent on transported ozone and ODS and their photochemistry, and especially the different
310 dynamics and chemistry in the Arctic and Antarctic regions.
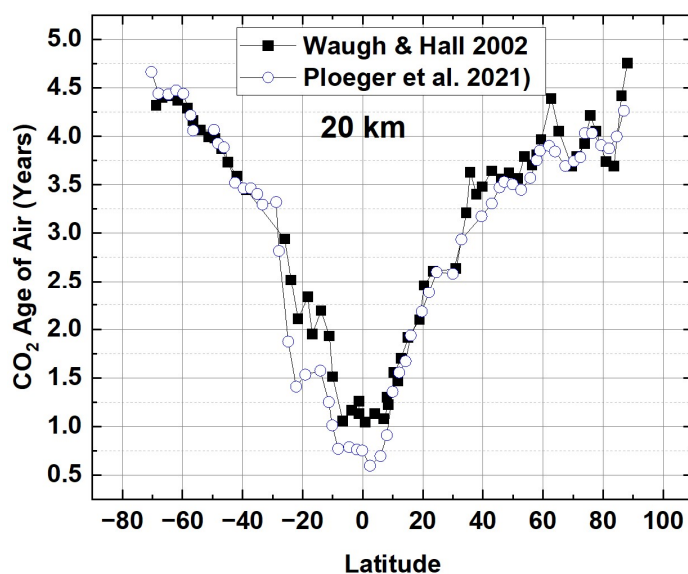
Fig. 11 Age of air derived from CO_2 data (Waugh and Hall, 2002; Ploeger et al., 2021)

311

312

313

314

315

316

317

3.0 Summary

319   The monthly averaged Merged Ozone Data set Ω_{MOD} (2.5^O latitude bands, 77.5^{O}S to 77.5^{O}N) from 1979
320   to 2021 were averaged into 10° latitude bands 75°S < θ < 75°N. A smoothed Ω_{MOD} version based on
321   Lowess(0.3) was used to determine the approximate dates of the latitude dependent ozone end of
322   ozone decrease date $T_A(\theta)$ ranging from 1994 to 1998 with an error estimate of ±0.5 years. The
323   systematic hemispherically asymmetric latitude dependent pattern $T_A(\theta)$ should appear in atmospheric
324   models that combine the effects of volcanic eruptions, photochemistry, and dynamics in their estimate
325   of the end of ozone decrease. The hemispheric asymmetry is caused by the formation of the annual
326   Spring Antarctic ozone (monthly spring average about 155 DU) hole with persistent isolating polar vortex
327   winds followed by the summer mixing with mid-latitude ozone rich air (December average about 300
328   DU). The Arctic region does not form a large spring ozone hole, nor does it have sustained isolating polar
329   vortex winds. Instead at 75°N (Fig. 1) it has the highest amount of monthly average winter ozone
330   450±25 DU that decreases to 290±20 DU monthly average during the summer. Trends of ozone $P_D(\theta)$ in
331   percent per decade were computed before and after the latitude dependent $T_A(\theta)$ using two different
332   methods, MLR and annual averages, that closely agree over their mutual latitude range of validity, 65°S
333   to 65°N. The annual average method can extend into polar latitudes. The most dramatic rates of ozone
334   loss were P_D = -10.9±3.6% decade at 77.5^{O}S and -8.0±1.1%/decade at 65°S, which is about double the
335   rate of loss of P_D = -5.7±4 %/decade at 77.5^{O}N and -4.4±1.2% per decade at 65°N. During the period
336   after T_A to 2021, there has been a small increase at latitudes in the SH from 25°S to 65°S with the largest
337   value being 1.6±1.4% per decade at 65°S. Aside from the small increases in the SH region there has been
338   no statistically significant ozone recovery toward 1979 values, just an almost constant ozone amount
339   after $T_A(\theta)$. The largest annual rate of ozone decrease occurred near the beginning of the SBUV data
340   record, 1979, showing large high latitude losses of -20.6 %/Year at 75°S caused by the springtime
341   Antarctic ozone hole compared to a smaller Arctic loss of -9.9%/Year at 75°N. During the period 2010 to
342   2021, there has been a small apparent decrease in ozone amount in Ω_{MOD} that is not yet statistically
343   significant at the 2-standard deviation level. A comparison between Ω_{MOD} and MLS stratospheric column
344   ozone shows small systematic negative differences in 2020 that mostly recovered in 2021 except near
345   the equator. This suggests that there is no statistically significant instrumental calibration drift between
346   Ω_{MOD} TCO and MLS stratospheric ozone.

347

348

349 **Appendix**

350 The MOD TCO data record since 2018 is obtained from OMPS-NP, which appears to show decreasing

351 TCO (Fig. 6). Because of this, the deseasonalized Ω_{MOD} are compared with MLS (Microwave Limb

352 Sounder) deseasonalized stratospheric column ozone for the period 2004 to 2021 to look for calibration

353 drifts in the Ω_{MOD} time series. The question addressed here is not the absolute agreement between Ω_{MOD}

354 and the MLS mostly stratospheric ozone column, but rather if there is a systematic drift between the

355 two data sets after 2016. Figures A1 and A2 show that the difference between the two deseasonalized

356 time series for latitudes from 65°S to 65°N and for the entire period 2005 – 2021. Of interest is the

357 period 2016 to 2021 when Ω_{MOD} was derived using NOAA-19 SBUV plus OMPS-NP 2016 – 2018 and from

358 OMPS-NP since 2018.
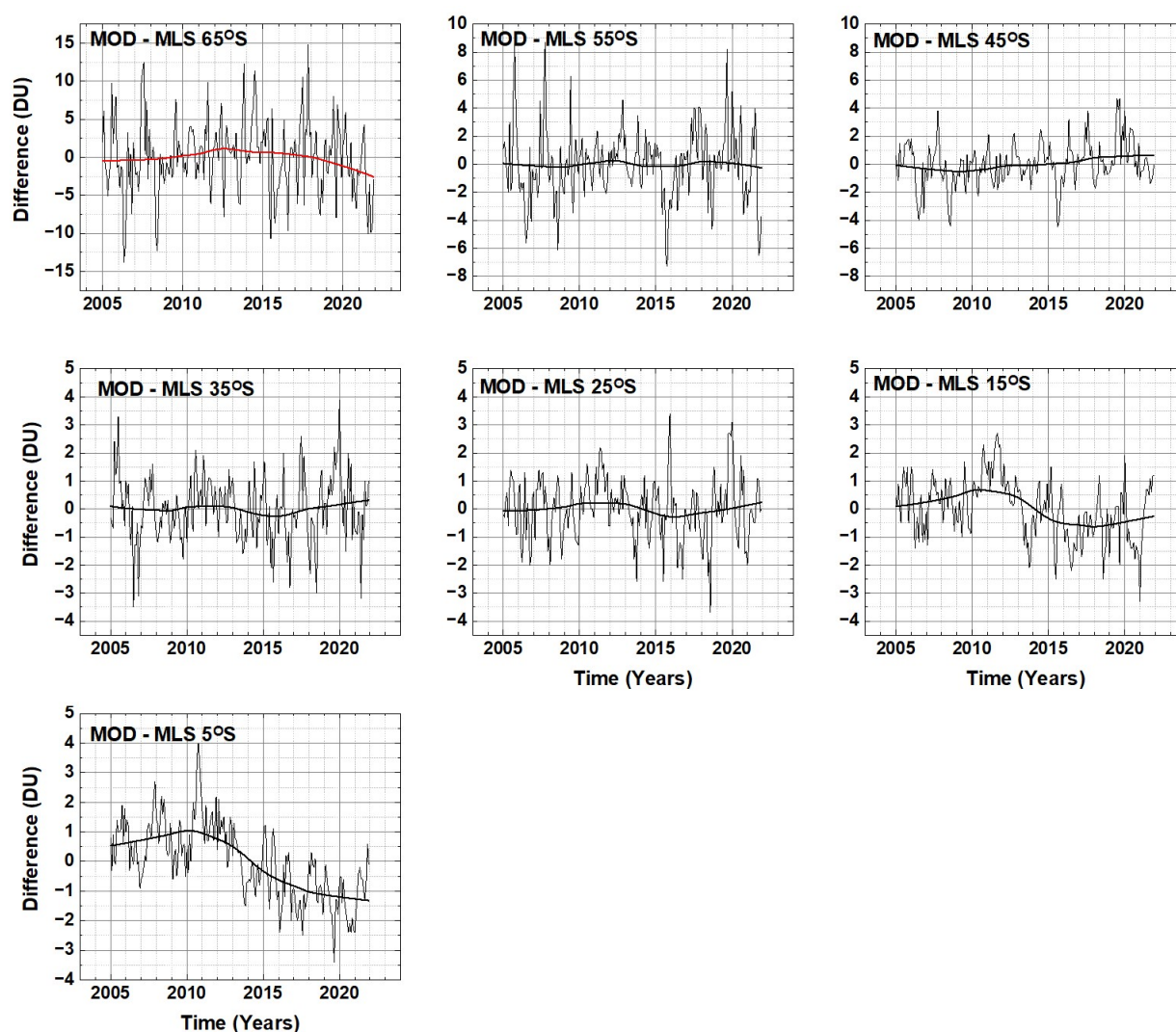
Fig. A1 A comparison of deseasonalized Ω_{MOD} with deseasonalized MLS stratospheric column ozone for 65°S to 5°S.

359

360
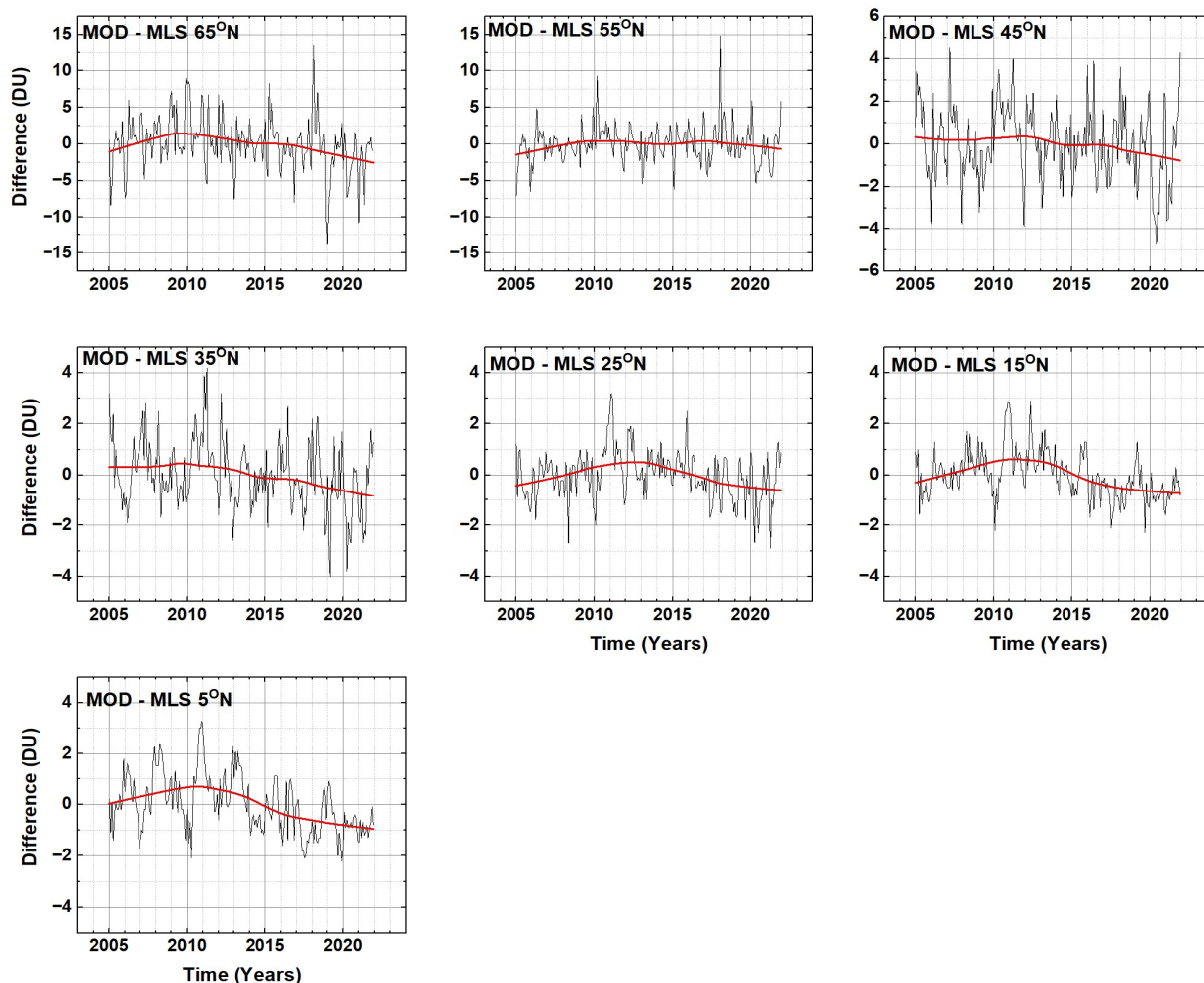
Fig. A2 A comparison of deseasonalized MOD total ozone with deseasonalized MLS stratospheric
column ozone for 5°N to 65°N. Variations of ±3DU are within the MOD merged record uncertainties.

361

362   The differences in Figs A1 and A2 between Ω_{MOD} and MLS since 2016 are not statistically significant at

363   the 2σ level. Variations of ± 3DU are within the Ω_{MOD} merged record uncertainties.

364

365   Since both MOD and MLS time series were deseasonalized, the mean values would be zero unless there

366   were changes in tropospheric ozone or instrument calibration drift. The differences are summarized in

367   Fig. A3 along with the 2σ', (σ' = standard deviation from the mean) error bars estimated from the

368   average of each deseasonalized time series. In 2020 there appears to be a systematic change in <MOD −

369   MLS> that may be a reduction in tropospheric ozone amount of about 3 DU caused by the economic

370   slowdown associated with COVID-19 (Ziemke et al, 2022). The systematic change mostly recovered in

371   2021 (Fig. A3) except for -1DU near the equator (-5°S to 15°N).
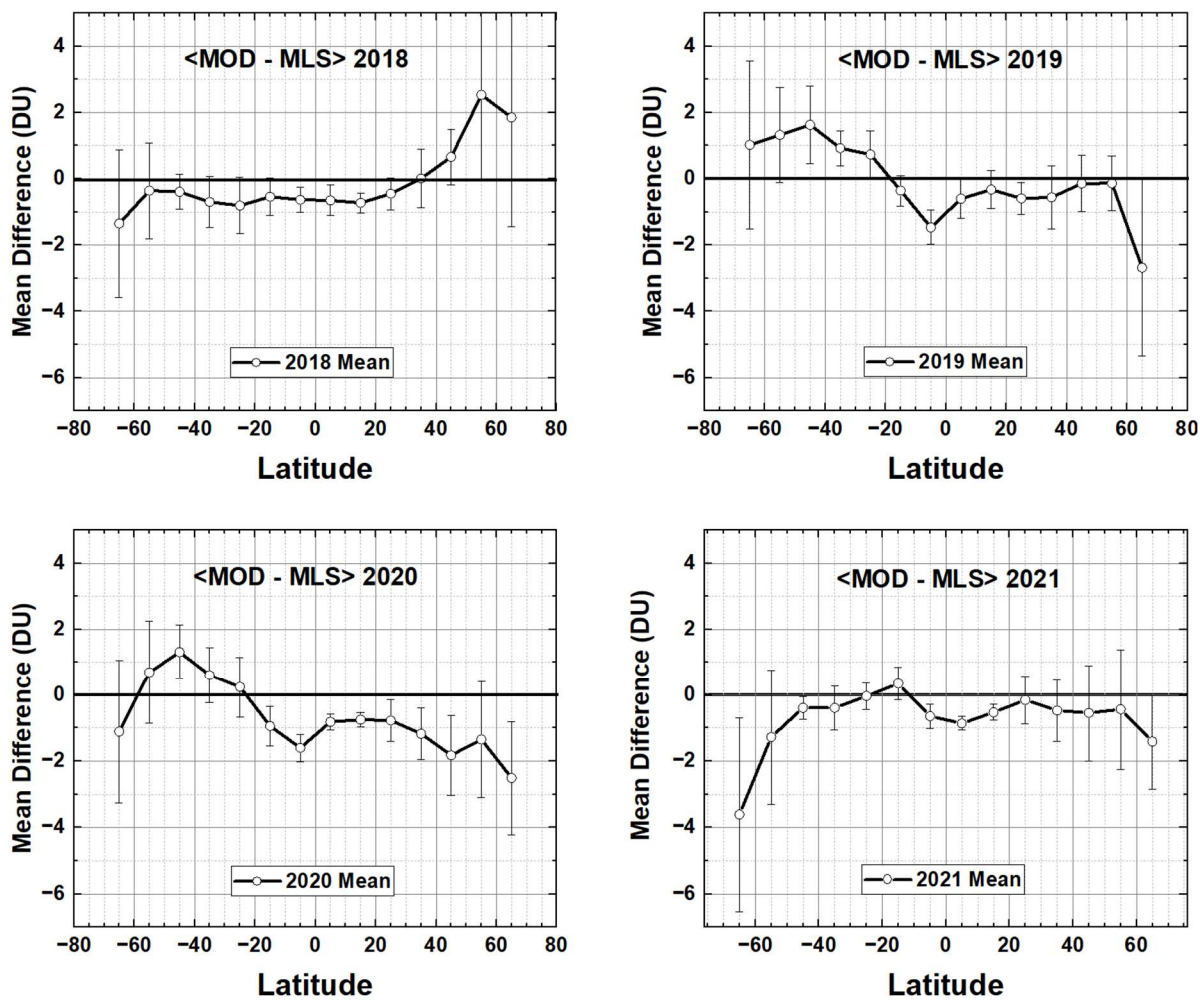
Fig. A3 Annual average <MOD – MLS> for the years 2018 to 2021. Error bars are 2σ', where σ' = standard error of the mean estimated from the average of the deseasonalized time series for each year shown in Figs. A1 and A2.

372

373

374   **4.0 References**

375   Bai, K., N.-B. Chang, R. Shi, H. Yu, and W. Gao, An intercomparison of multidecadal observational and
376   reanalysis data sets for global total ozone trends and variability analysis, J. Geophys. Res. Atmos., 122,
377   7119–7139, doi:10.1002/2016JD025835, 2017.

378   Bhartia, P. K. , R. D. McPeters, L. E. Flynn, S. Taylor, N. A. Kramarova, S. Frith, B. Fisher, and M. DeLand,
379   Solar Backscatter UV (SBUV) total ozone and profile algorithm. Atmos. Meas. Tech., 6, 2533–2548,
380   doi:10.5194/amt-6-2533-2013, 2013.

381   Bodeker, G. E. and Kremser, S.: Indicators of Antarctic ozone depletion: 1979 to 2019, Atmos. Chem.
382   Phys., 21, 5289–5300, https://doi.org/10.5194/acp-21-5289-2021, 2021.

383   Brewer, A. W., Evidence for a world circulation provided by the measurements of helium and water
384   vapour distribution in the stratosphere, Quarterly Journal of the Royal Meteorological Society. 75 (326):
385   351–363. Bibcode:1949QJRMS..75..351B. doi:10.1002/qj.49707532603. ISSN 1477-870X, 1949.

386   Crutzen, P. J. and Arnold, F.: Nitric acid cloud formation in the cold Antarctic stratosphere: a major cause
387   for the springtime "ozone hole", Nature, 342, 651–655, https://doi.org/10.1038/324651a0, 1986.

388   Dameris, Martin and Mark P. Baldwin, Impact of Climate Change on the Stratospheric Ozone Layer,
389   Stratospheric Ozone Depletion and Climate Change, Edited by Rolf Muller, Chapter 8, 214-252, Royal
390   Society of Chemistry 2012.

391   Dobson, G. M. B.; Harrison, D. N.; Lindemann, F. A., Measurements of the amount of ozone in the Earth's
392   atmosphere and its relation to other geophysical conditions, Proceedings of the Royal Society of London.
393   Series A, Containing Papers of a Mathematical and Physical Character. 110 (756): 660–693.
394   Bibcode:1926RSPSA.110..660D. doi:10.1098/rspa.1926.0040. 1926.

395   Butchart, N., The Brewer-Dobson circulation, Rev. Geophys.,52, 157–184, doi:10.1002/2013RG000448,
396   2014.

397   Cleveland, W.S., Robust Locally Weighted Regression and Smoothing Scatterplots, Journal of the
398   American Statistical Association, Vol. 74, pp. 829-836, https://doi.org/10.2307/2286407, 1979.
399
400   Cleveland, W.S. and Devlin, S.J., Locally Weighted Regression: An Approach to Regression Analysis by
401   Local Fitting," Journal of the American Statistical Association, Vol. 83, pp. 596-610,
402   DOI: 10.1080/01621459.1988.10478639 1988.
403
404   DeLand, M. T., S. L. Taylor, L. K.Huang, and B. L. Fisher, Calibration of the SBUV version 8.6 ozone data
405   product, Atmos. Meas. Tech., 5, 2951–2967, doi:10.5194/amt-5-2951-2012, 2012.
406
407   Frith, S. M., N. A. Kramarova, R. S. Stolarski, R. D. McPeters, P. K. Bhartia, and G. J. Labow, Recent
408   changes in total column ozone based on the SBUV Version 8.6 Merged Ozone Data Set, J. Geophys. Res.
409   Atmos., 119, 9735-9751, doi:10.1002/2014JD021889, 2014.

410 Frith, S. M., Stolarski, R. S., Kramarova, N. A., and McPeters, R. D.: Estimating uncertainties in the SBUV
411 Version 8.6 merged profile ozone data set, Atmos. Chem. Phys., 17, 14695–14707,
412 https://doi.org/10.5194/acp-17-14695-2017, 2017.

413 Frith, S. M., Bhartia, P. K., Oman, L. D., Kramarova, N. A., McPeters, R. D., and Labow, G. J.: Model-based
414 climatology of diurnal variability in stratospheric ozone as a data analysis tool, Atmos. Meas. Tech., 13,
415 2733-2749, https://doi.org/10.5194/amt-13-2733-2020, 2020.
416
417 Guttman, I., Linear Models, An Introduction, 358 pp., Wiley-Interscience, New York, 1982.

418 Herman, J.R., R. McPeters, D. Larko, Ozone depletion at northern and southern latitudes derived from
419 January 1979 to December 1991 Total Ozone Mapping Spectrometer data, 98, 13783-12793
420 https://doi.org/10.1029/93JD00601, 1993.

421 Khosrawi, F., Urban, J., Pitts, M. C., Voelger, P., Achtert, P., Kaphlanov, M., Santee, M. L., Manney, G. L.,
422 Murtagh, D., and Fricke, K.-H.: Denitrification and polar stratospheric cloud formation during the Arctic
423 winter 2009/2010, Atmos. Chem. Phys., 11, 8471–8487, https://doi.org/10.5194/acp-11-8471-2011,
424 2011.

425 Linz, Marianna, R. Alan Plumb, Edwin P. Gerber, Aditi Sheshadri, The Relationship between Age of Air
426 and the Diabatic Circulation of the Stratosphere. J. Atmos. Sci., 73, 4507-4518, doi: 10.1175/JAS-D-16-
427 0125.1, 2016.

428 McPeters, R. D., P. K. Bhartia, D. Haffner, G. J. Labow, and L. Flynn, The version 8.6 SBUV ozone data
429 record: An overview, J. Geophys. Res. Atmos., 118, 8032-8039, doi:10.1002/jgrd.50597., 2013.

430 Newman, P.A., S. R. Kawa, E. R. Nash, On the size of the Antarctic ozone hole, Geophys. Res. Lett., 1-4,
431 31, doi:10.1029/2004GL020596, 2004.

432 Newman, P. A., Daniel, J. S., Waugh, D. W., and Nash, E. R., A new formulation of equivalent effective
433 stratospheric chlorine (EESC), Atmos. Chem. Phys., 7, 4537–4552, https://doi.org/10.5194/acp-7-4537-
434 2007, 2007.

435 Oldenborgh, Geert Jan van, Harry Hendon, Timothy Stockdale, Michelle L'Heureux, Erin Coughlan de
436 Perez, Roop Singh, and Maarten van Aalst, Defining El Niño indices in a warming climate, Environ. Res.
437 Lett. 16 044003, DOI 10.1088/1748-9326/abe9ed, 2021.

438 Randel, W. J., and J. B. Cobb, Coherent variations of monthly mean total ozone and lower stratospheric
439 temperature, J. Geophys. Res., 99, 5433--5447, DOI:10.1029/93JD03454, 1994.

440 Solomon, S., Garcia, R. R., Rowland, F. S., and Wuebbles, D. J.: On the depletion of Antarctic ozone,
441 Nature, 321, 755–758, https://doi.org/10.1038/321755a0, 1986.

442 Solomon, S., Stratospheric ozone depletion: a review of concepts and history, Rev. Geophys., 37, 275–
443 316, https://doi.org/10.1029/1999RG900008, 1999.

444 Solomon, S., Portmann, R. W., & Thompson, D. W., Contrasts between Antarctic and Arctic ozone

445   depletion. Proceedings of the National Academy of Sciences, 104(2), 445-449.
446   https://doi.org/10.1073/pnas.0604895104, 2007.

447   Solomon, Susan, Diane J. Ivy, Doug Kinnison, Michael J. Mills, Ryan R. Neely, Iii, And Anja Schmidt,
448   Emergence of healing in the Antarctic ozone layer, Vol 353, 269-274 DOI: 10.1126/science.aae0061,
449   2016.

450   Staehelin, J., N. Harris, C. Appenzeller, and J. Eberhard, Ozone trends: A review, REV GEOPHYS., 39,231-
451   290, 10.1029/1999RG000059, 2001.

452   Stolarski R. D., P. Bloomfield, R. D. McPeters, and J. R. Herman, Total ozone trends deduced from
453   Nimbus 7 TOMS data, Geophys., Res., Lett., 18, https://doi.org/10.1029/91GL01302, 1991.

454   Stolarski R, Bojkov R, Bishop L, Zerefos C, Staehelin J, Zawodny J. Measured trends in stratospheric
455   ozone, Science, Apr 17;256(5055):342-9. doi: 10.1126/science.256.5055.342. PMID: 17743110, 1992.
456
457   Stone, K. A., Solomon, S., and Kinnison, D. E., On the identification of ozone recovery. Geophysical
458   Research Letters, 45, https://doi.org/10.1029/2018GL077955, 2018.
459
460   Stone KA, Solomon S, Kinnison DE, Mills MJ. On Recent Large Antarctic Ozone Holes and Ozone Recovery
461   Metrics. Geophys Res Lett. 2021 Nov 28;48(22):e2021GL095232. doi: 10.1029/2021GL095232. Epub
462   2021 Nov 18. PMID: 35864979; PMCID: PMC9286815.
463
464   Strahan, S. E., and Douglass, A. R., Decline in Antarctic ozone depletion and lower stratospheric chlorine
465   determined from Aura Microwave Limb Sounder observations. Geophysical Research Letters, 45, 382–
466   390. https://doi.org/10.1002/2017GL074830, 2018.
467
468   Tritscher, I., Pitts, M. C., Poole, L. R.,Alexander, S. P., Cairo, F., Chipperfield, M. P., et al. (2021). Polar
469   stratospheric clouds: Satellite observations, processes, and role in ozone depletion. Reviews of
470   Geophysics, 59, e2020RG000702. https://doi.org/10.1029/2020RG000702, 2021.

471   Velders, G. J., & Andersen, S. O. (2018). The Montreal Protocol on Substances that Deplete the Ozone
472   Layer and its amendments: An overview. Air Pollution and Health, 11-28, 2018.

473   Wallace, J. M., R. L. Panetta, and J. Estberg, Representation of the equatorial stratospheric quasi-biennial
474   oscillation in EOF phase space, J. Atmos. Sci., 50, 1751--1762, https://doi.org/10.1175/1520-
475   0469(1993)050<1751:ROTESQ>2.0.CO;2, 1993.
476
477   Weatherhead, E. C., Reinsel, G. C., Tiao, G. C., Meng, X.-L., Choi, D., Cheang, W.-K., Keller, T., DeLuisi, J.,
478   Wuebbles, D. J., Kerr, J. B., Miller, A. J., Oltmans, S. J., and Frederick, J. E.: Factors affecting the
479   detection of trends: Statistical considerations and applications to environmental data, 103,17149–
480   17161, https://doi.org/10.1029/98JD00995, 1998.
481
482   Waugh, D.W. and Hall, T.M., Age of stratospheric air: theory, observations, and models, Rev. of
483   Geophys., 40,1-10, doi:10.1029/2000RG000101, 2002.
484   Weber, Mark, Carlo Arosio, Melanie Coldewey-Egbers, Vitali E. Fioletov, Stacey M. Frith, Jeannette D.
485   Wild, Kleareti Tourpali, John P. Burrows, and Diego Loyola, Global total ozone recovery trends attributed

486   to ozone-depleting substance (ODS) changes derived from five merged ozone datasets,
487   https://doi.org/10.5194/acp-22-6843-2022, ACP, 22, 6843–6859, 2022.

488

489   World Meteorological Organization (WMO), Scientific Assessment of Ozone Depletion: 2022, GAW
490   Report No. 278, 509 pp., WMO, Geneva, 2022.

491   Ziemke, Jerry R. Luke D. Oman, Sarah A. Strode, Anne R. Douglass, Mark A. Olsen, Richard D.
492   McPeters, Pawan K. Bhartia, Lucien Froidevaux, Gordon J. Labow, Jacquie C. Witte, Anne M.
493   Thompson, David P. Haffner, Natalya A. Kramarova, Stacey M. Frith, Liang-Kang Huang, Glen R.
494   Jaross, Colin J. Seftor, Mathew T. Deland, Steven L. Taylor, Trends in global tropospheric ozone inferred
495   from a composite record of TOMS/OMI/MLS/OMPS satellite measurements and the MERRA-2 GMI
496   simulation, Atmospheric Chemistry and Physics, 10.5194/acp-19-3257-2019, **19**, 5, (3257-3269), 2019.

497   Ziemke, J. R., N. A. Kramarova, S. M. Frith, L.-K. Huang, D. P. Haffner, K. Wargan, L. N. Lamsal, G. J.
498   Labow, R. D. McPeters, and P. K. Bhartia, NASA satellite measurements show global-scale reductions in
499   tropospheric ozone in 2020 and again in 2021 during COVID-19, Geophys. Res. Lett.,
500   49, https://doi.org/10.1029/2022GL098712, 2022.

501

502   **Author contribution**:

503   Jay Herman is responsible for writing the text, the annual integral trend calculations, and all the
504   figures. Jerald Ziemke supplied the MLR trend calculations and the comparison with MLS. Richard
505   McPeters supplied the MOD ozone as a continuous function of time from 1979 to 2021 for each
506   latitude band.

507   **Data Availability**
508   The original data used are publicly available in an ASCII format**.**
509   https://acd-ext.gsfc.nasa.gov/Data_services/merged/
510   and processed data in Excel format
511   https://avdc.gsfc.nasa.gov/pub/DSCOVR/JayHerman/MOD_Ozone_Trends/
512
513
514   **Competing interests**:
515   The authors declare that they have no conflict of interest.

516

517

518

519

520   **Acknowledgements**:
521   The authors want to acknowledge the contribution and help of Stacey Frith for compiling the SBUV
522   and OMPS-NP data sets to produce the long ozone data record. She also reviewed the paper and
523   added some important corrections.

524

525 **Figure Captions xxx**

526 Fig. 1 Left: The zonally and monthly averaged Ω_{MOD} data set 1979 – 2021 and -77.5^O to 77.5^O. Right: Time
527 and zonal averaged ozone and its maxima and minima 1979 – 2021. Error bars are 1 standard deviation
528 ±1σ.

529 Fig. 2 The latitude average residual term from Eq. 1 in percent 100 <R(t,q_i)/W_{MOD}(t,q_i)> The black line is
530 the Lowess(0.1) fit (Cleveland, 1979) to the R(t,q) with an average error estimate of ±2%. The light-
531 colored lines are each latitude's R(t,q) in a hemisphere $0^O < \theta < 65^O$.

532 Fig. 3 The ozone trend $P_D(\theta)$ for the entire period 1979 – 2021 for two methods, MLR and Annual
533 Average. The latitude grids for the two methods are offset to show the agreement in the trends and 2σ
534 error bars.

535 Fig. 4. A. Ω_{MOD} time series for θ = 5°N and 5°S. B. The deseasonalized TCO time series for θ = 5°N and
536 5°S without removing QBO effects (Eq. 1). The approximate dates are shown of volcanic eruptions that
537 injected large amounts of SO_2 into the stratosphere leading to minima approximately 1 year later.

538 Fig. 5 Ω_{MOD} in four latitude bands and Lowess(0.3) fitting functions (f = 0.3, black lines). Examples of
539 different f = 0.1 (Red) and 0.05 (blue dots) are shown at 45°S and 45°N. Note the slight downturn since
540 2010 in the Lowess(0.3) at 45°N and 55°N.

541 Fig. 6 Lowess(0.3) fits to the Ω_{MOD} data for 16 latitude bands used to determine $T_A(\theta)$. Note that the
542 ozone scale varies for each latitude.

543 Fig 7 Turnaround dates $T_A(\theta)$ as a function of latitude from Fig.6 with an estimated accuracy of ±0.5
544 years based on the analysis in Fig. 5.

545 Fig. 8a Ozone trends $P_D(\theta)$ (percent per decade) using the MLR and Annual Average methods before and
546 after $T_A(\theta)$. 6b A magnified version of the MLR estimated trends after T_A with 2σ uncertainties.

547 Fig. 9 The percent change in ozone per year in 1979 or 1980

548 Fig. 10 Ozone trends $P_D(\theta)$ (Percent per Decade) for the period 2010 – 2021 for the Annual Average and
549 MLR methods applied to Ω_{MOD}(t,θ).

550 Fig. 11 Age of air derived from CO_2 data (Waugh and Hall, 2002; Ploeger et al., 2021)

551

552   **Figures**
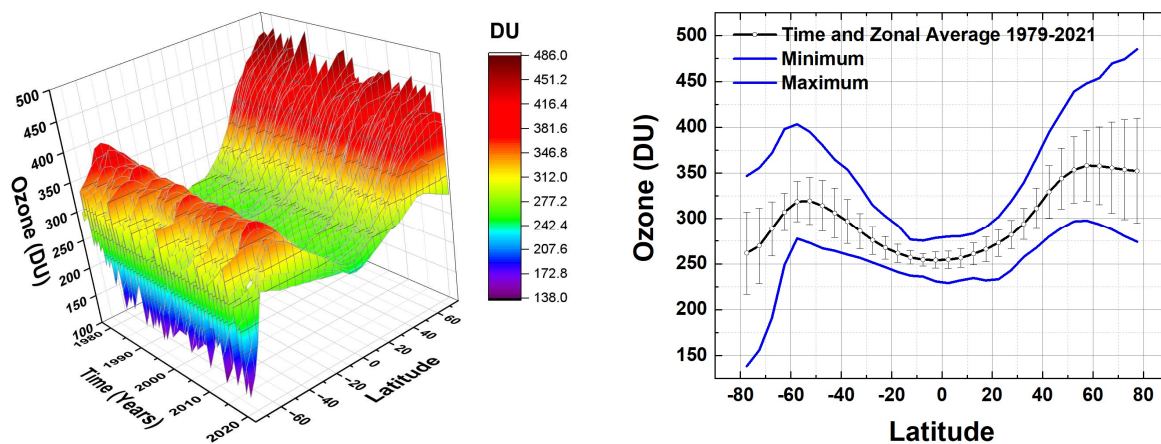
Fig. 1 Left: The zonally and monthly averaged Ω_{MOD} data set 1979 – 2021 and -77.5^O to 77.5^O. Right: Time and zonal averaged ozone and its maxima and minima 1979 – 2021. Error bars are 1 standard deviation ±1σ.

553   **F01**

554

555
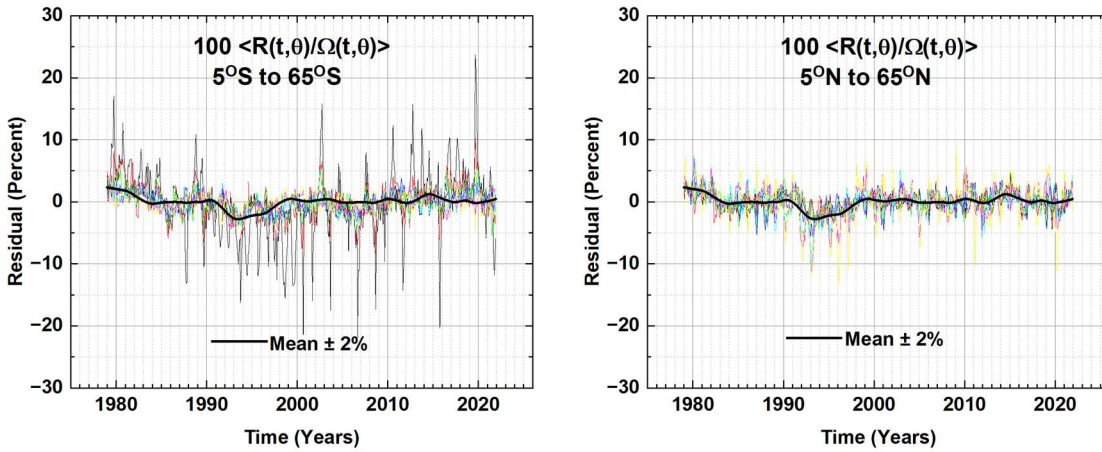
Fig. 2 The latitude average residual term from Eq. 1 in percent 100 $<R(t,q_i)/W_{MOD}(t,q_i)>$ The black line is the Lowess(0.1) fit (Cleveland, 1979) to the R(t,q) with an average error estimate of ±2%. The light-colored lines are each latitude's R(t,q) in a hemisphere $0^O < \theta < 65^O$.

556

557

558   **F02**

559

Fig. 3 The ozone trend $P_D(\theta)$ for the entire period 1979 – 2021 for two methods, MLR and Annual Average. The latitude grids for the two methods are offset to show the agreement in the trends and 2σ error bars.

560

561   **F03**

562
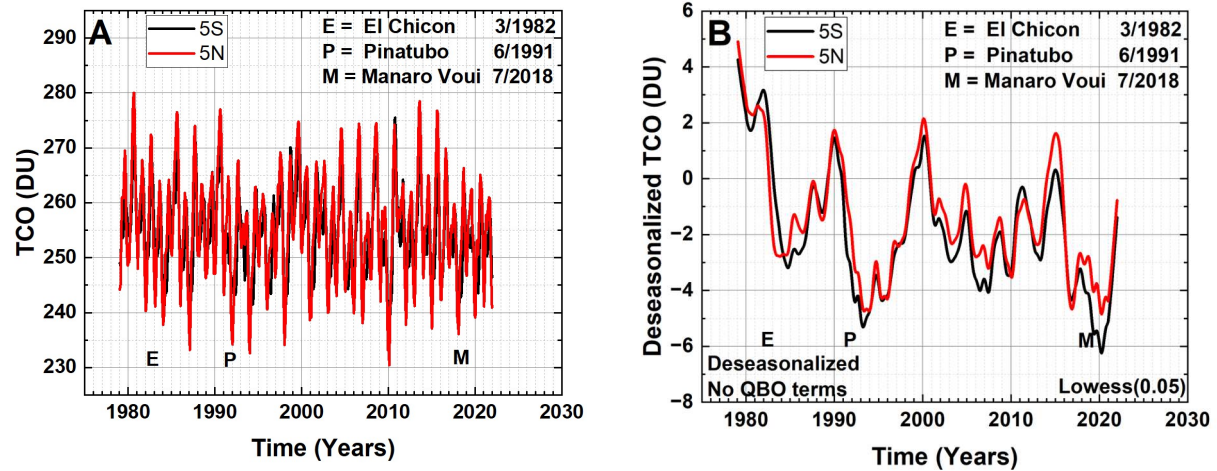
Fig. 4. A. Ω_{MOD} time series for $\theta = 5^O$N and 5^OS. B. The deseasonalized TCO time series for $\theta = 5^O$N and 5^OS without removing QBO effects (Eq. 1). The approximate dates are shown of volcanic eruptions that injected large amounts of SO_2 into the stratosphere leading to minima approximately 1 year later.

563

564   **F04**

565
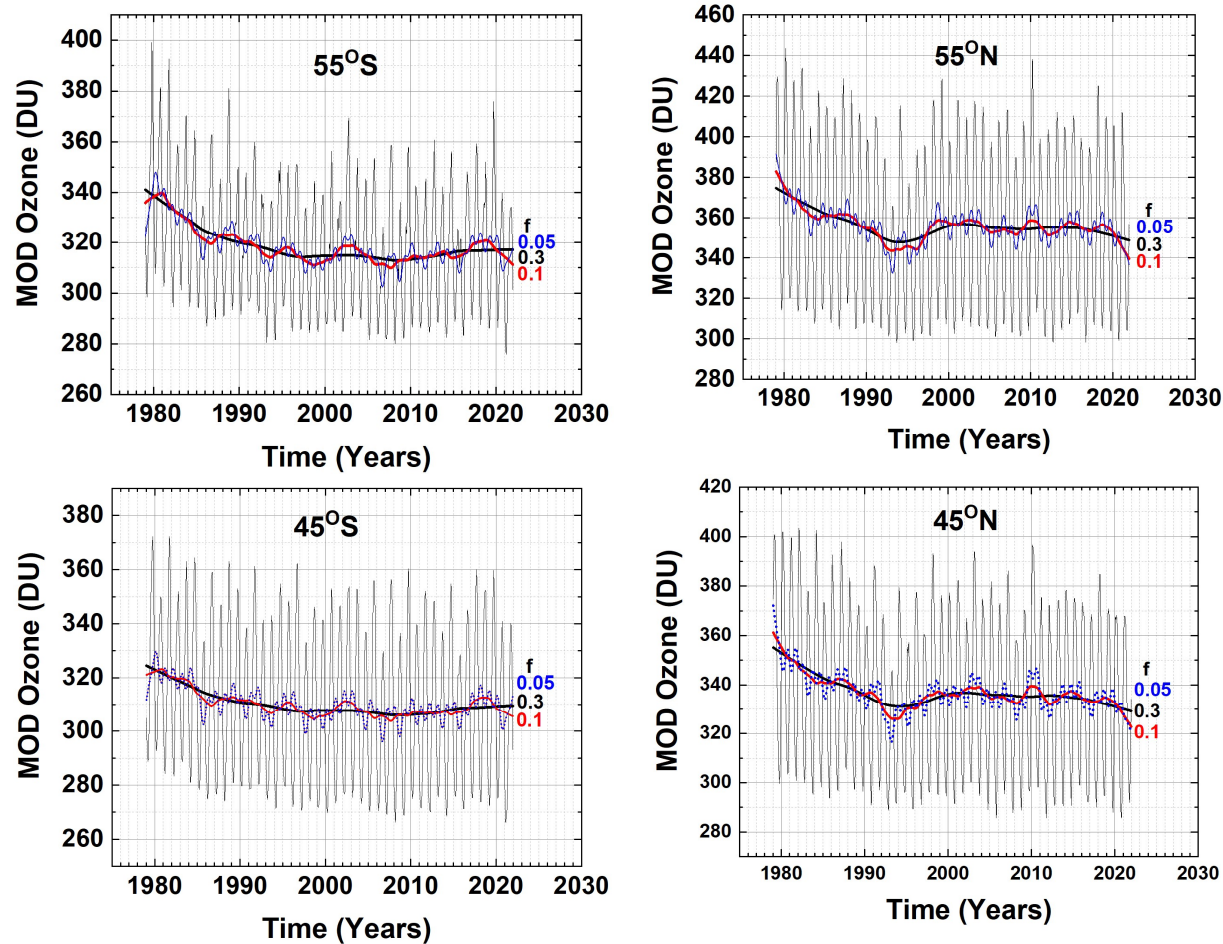
Fig. 5 Ω_{MOD} in four latitude bands and Lowess(0.3) fitting functions (f = 0.3, black lines). Examples of different f = 0.1 (Red) and 0.05 (blue dots) are shown at 45°S and 45°N. Note the slight downturn since 2010 in the Lowess(0.3) at 45°N and 55°N.

566

567   **F05**

568
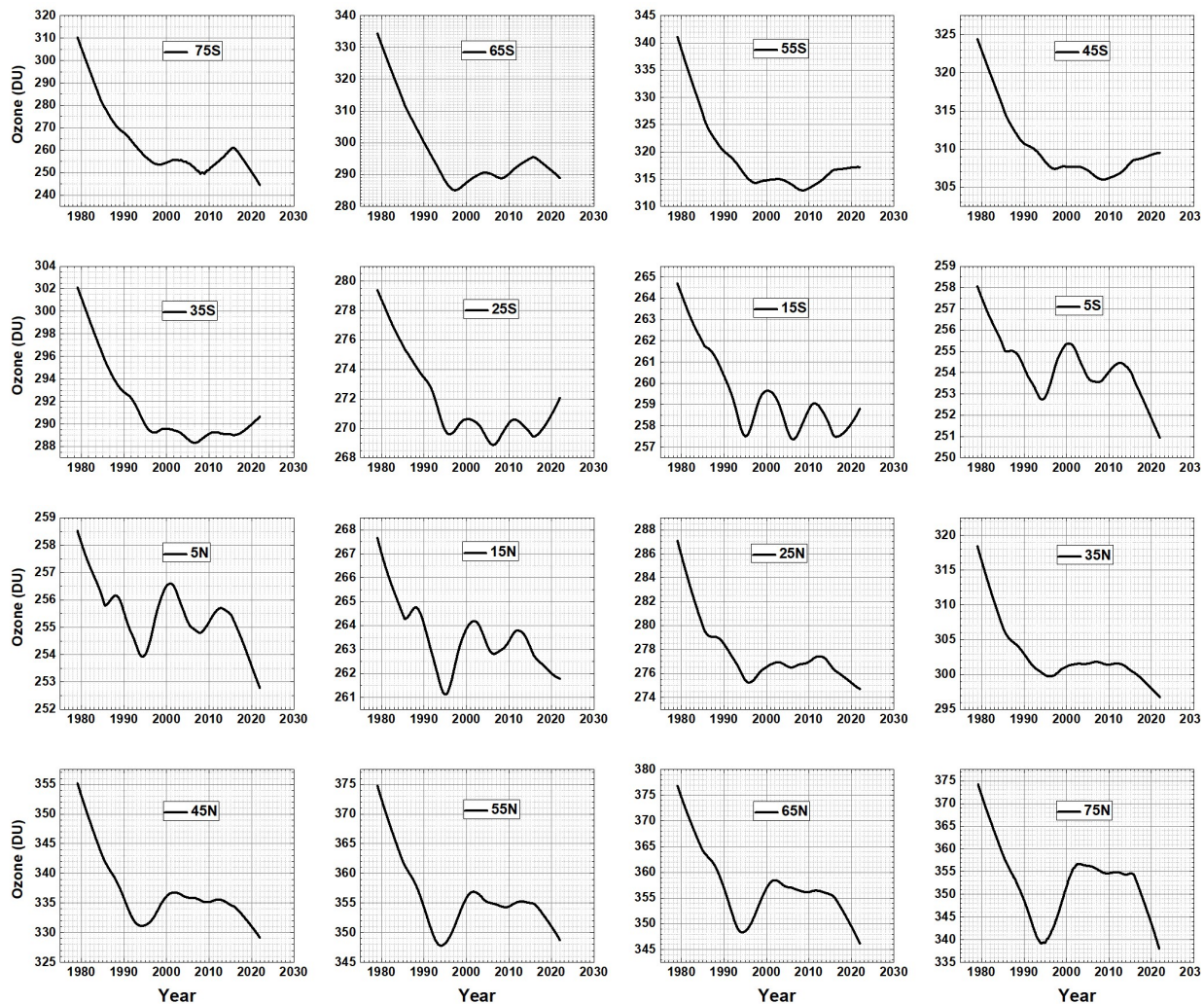
Fig. 6 Lowess(0.3) fits to the Ω_{MOD} data for 16 latitude bands used to determine $T_A(\theta)$. Note that the ozone scale varies for each latitude.

569

570 **F06**

571

572
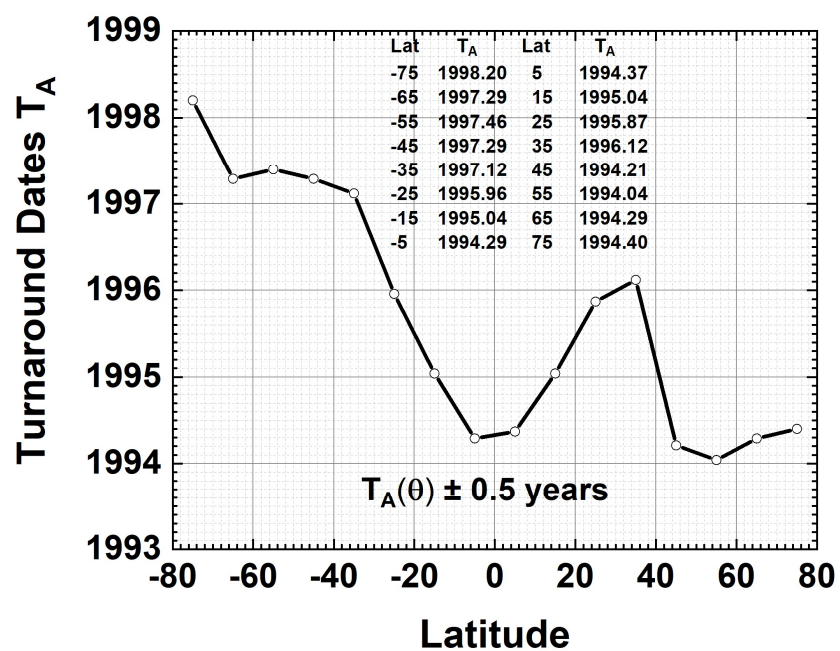
Fig 7 Turnaround dates $T_A(\theta)$ as a function of latitude from Fig.6 with an estimated accuracy of ±0.5 years based on the analysis in Fig. 5.

573

574 **F07**

575
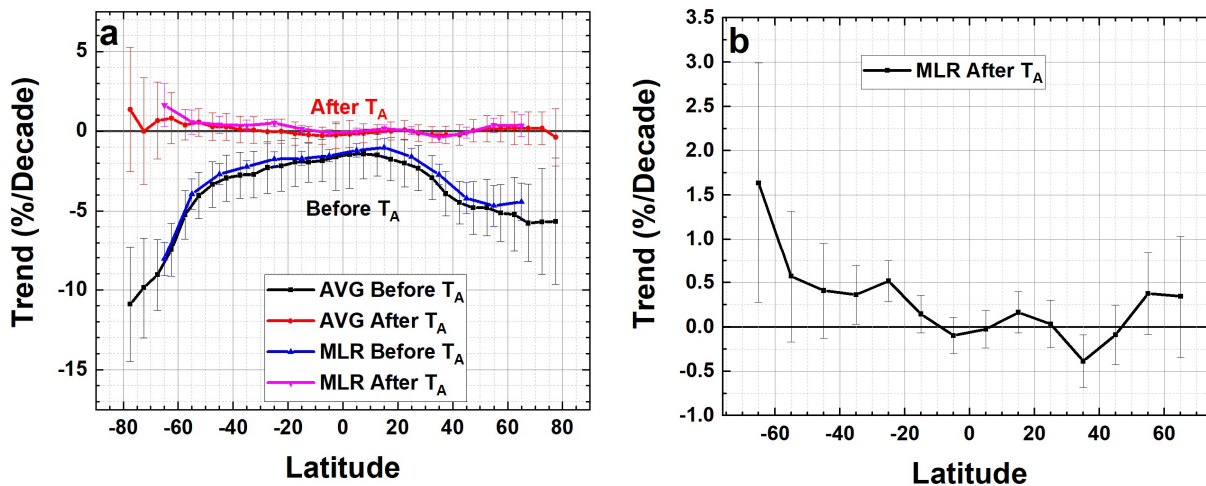
Fig. 8a Ozone trends $P_D(\theta)$ (percent per decade) using the MLR and Annual Average methods before and after $T_A(\theta)$. 6b A magnified version of the MLR estimated trends after T_A with 2σ uncertainties.

576

F08

578
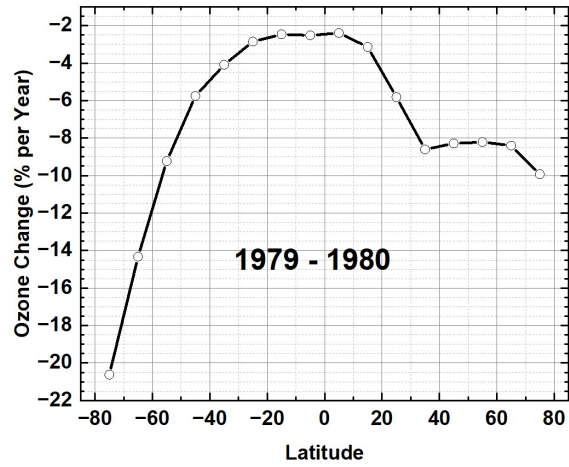
Fig. 9 The percent change in ozone per year in 1979 or 1980

579
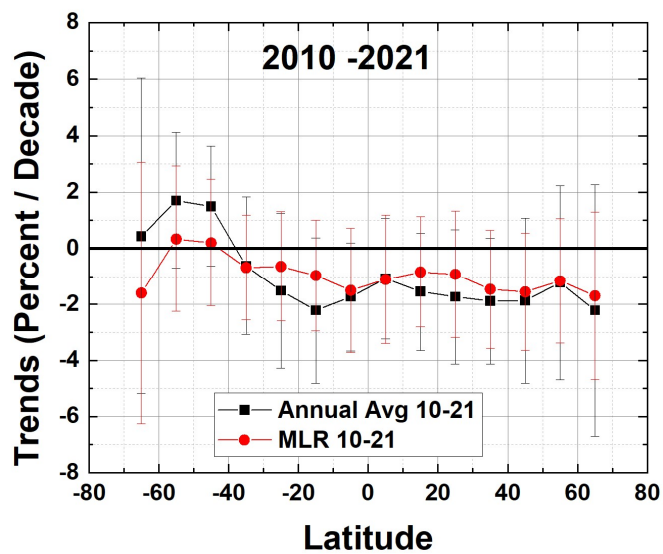
F09

581

Fig. 10 Ozone trends $P_D(\theta)$ (Percent per Decade) for the period 2010 – 2021 for the Annual Average and MLR methods applied to $\Omega_{MOD}(t,\theta)$.

582

F10

584
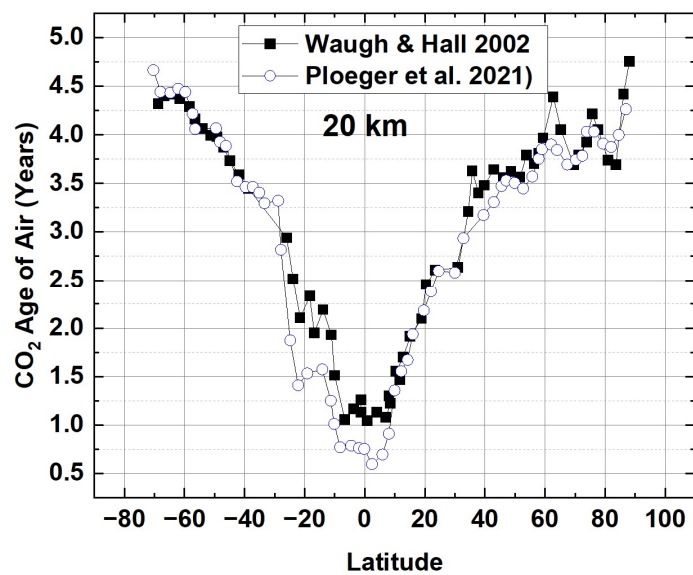
Fig. 11 Age of air derived from CO_2 data (Waugh and Hall, 2002; Ploeger et al., 2021)

585

586   **F11**